CHEMISTRY OF MATERIALS

pubs.acs.org/cm

Article

Solid−Solid Phase Change Layered Hybrid Materials for Thermal Energy Storage: Impact of the Chemical Composition and Structural Topology

Côme Archinard, Ali Saad, Hubert Chevreau, Jean-Yves Mevellec, Bernard Humbert, Xavier Biquard, Erik Elkaïm, Kenneth Paul Marshall, Dragos Constantin Stoian, Wouter Van Beek, Olivier Hernandez,* Grégory Largiller,* and Thomas Devic*

Cite This: *Chem. Mater.* 2026, 38, 2712−2726

Read Online

ACCESS | Metrics & More | Article Recommendations | Supporting Information

ABSTRACT: Solid−solid phase change materials (SS-PCMs) are attractive candidates for thermal energy storage (TES) owing to their intrinsic shape stability, yet their widespread application remains limited by the lack of design rules linking the molecular structure to phase-transition properties. Here, we present a comprehensive study of layered hybrid chlorometallates, $(C_nH_{2n+1}NH_3)_2MCl_4$ (M = Cu, Mn, Zn; n = 6−16), as tunable SS-PCMs. For that, 15 compounds (M = Cu, Mn, Zn; n = 6, 7, 12, 13, 16) were prepared, and their low-temperature (LT) forms were studied by single-crystal XRD and vibrational spectroscopies. By a multitechnique approach, involving calorimetry, temperature-dependent infrared, and Raman spectroscopies, and combined in a single synchrotron experiment temperature-dependent X-ray absorption spectroscopy (XAS), total scattering/Pair Distribution Function (PDF), and powder XRD (PXRD) analyses, we evidenced the impact of both parameters (M and n) not only on the LT structures but also on the thermal properties and on the high-temperature (HT) structures. Especially, we evidenced that although materials based on octahedrally (here Mn and Cu) and tetrahedrallly (here Zn) coordinated cations share many common features in their LT forms (alternating organic−inorganic layered structures, alkylammonium chains parallel to each other, and supramolecular organic−inorganic interactions of the same nature and strength), their HT phases strongly differ, especially at a medium range distance. This comprehensive study is not only of fundamental interest but will also help to address questions, such as the shaping and mechanical integrity of these SS-PCMs upon thermal cycling that need to be answered prior to their integration into practical devices for next-generation TES.

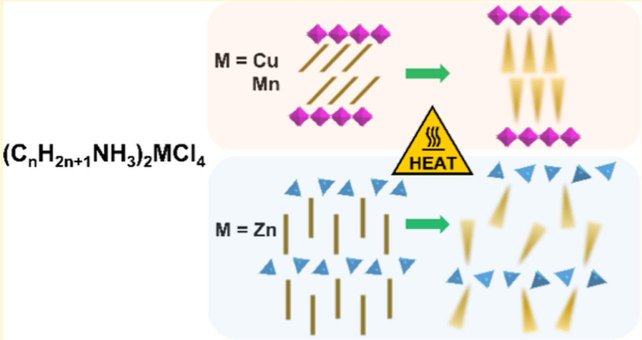

INTRODUCTION

Thanks to their versatile composition and structure, hybrid materials consisting of anionic halogenated metallic cations and organic cations are known to present very diverse properties, in the field of magnetism, luminescence, electric transport, ferroelectricity, and so on.[1−3] Among them, layered materials comprising alkylammonium cations formulated $(C_nH_{2n+1}NH_3)_2M^{II}Cl_4$ (M = Cd, Cu, Mn, Fe, Zn, Co; X = Cl, Br, I, n typically ≥4) were shown to systematically present one or more temperature- or pressure-induced solid−solid phase transition(s). Considering the reversibility and the energies involved in such transitions, seminal publications back in the 70's−80's have identified the promises of these solid−solid phase change materials (SS-PCMs) for thermal management and energy storage.[4−8] In line with the current needs for energy saving and more energy efficient processes, there is in the past decade a renewed interest for such materials.[9−17] These compounds present closely related crystal structures, consisting of alternating layers of organic and inorganic moieties, resulting from the segregation of the apolar alkyl chains and the polar units constituted by the ammonium heads interacting with anionic metal(II) tetrahalide through hydrogen bonds. Depending on M, the inorganic slabs consist of either a 2-D perovskite arrangement of MCl_6 octahedra (M = Cu, Cd, Mn, Fe) or isolated MCl_4 tetrahedra (M = Co, Zn), affecting the packing of the alkyl chains. Hence, their versatile composition (M, X, n can be modified at will) make these materials particularly tunable when compared to conventional organic SS-PCMs such as sugar alcohols.[18] Phase transitions in

Received: October 28, 2025
Revised: February 26, 2026
Accepted: March 2, 2026
Published: March 10, 2026

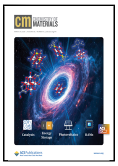

https://doi.org/10.1021/acs.chemmater.5c02855

these hybrid materials were primarily identified and studied by differential scanning calorimetry (DSC) and powder X-ray diffraction (PXRD).[7,19] While low-temperature (LT) crystal structures are rather easily available by single-crystal XRD (SCXRD), attempts to study the high-temperature (HT) phases by this technique were of little success,[11,12,20−26] as the mechanical strains associated with the structural transition led, in most cases, to a drastic degradation of the single crystals.[20,27] Analyses based on PXRD are also extremely challenging considering the large unit−cell parameters, often low symmetry, and peak broadening occurring upon transition; such analyses gave at best plausible unit−cell parameters and space groups. Even for the most successful cases, the authors evidenced the high dynamic disorder of the alkyl chains, rendering the refinement of a localized model for the HT states to be of limited significance. Hence, most structural information, especially related to the organic moieties, were gained on selected compositions from vibrational (infrared and Raman)[11,28−36] and nuclear spectroscopies (solid-state NMR[20,37−40] and NQR[20,37]) or incoherent neutron scattering.[41] It was proposed from these studies that the structural transitions involve the stepwise modification of the orientation and conformation of the alkyl chains, with the appearance of kink motifs (*gauche-trans-gauche* C−C−C−C sequences) to eventually reach a dynamically disordered state ("chain melting"), while the inorganic part is less impacted.[20,27]

In the present article, we systematically investigated a series of 15 solids formulated $(C_nH_{2n+1}NH_3)_2MCl_4$ with M = Cu, Mn, Zn and n = 6, 7, 12, 13, 16, later denoted $\mathbf{C_nM}$, with the aim at addressing the effect of the nature of the inorganic layer (2-D perovskite vs non perovskite for M = Cu, Mn and Zn, respectively), the geometry of the MCl_6 octahedra (regular and distorted for Mn and Cu, respectively), and of the length of the alkyl chains ($n \leq 7$ and $n \geq 12$, short and long, respectively). By a multitechnique approach, involving calorimetry, temperature-dependent infrared, and Raman spectroscopies, and combined in a single synchrotron experiment temperature-dependent short-range (X-ray absorption spectroscopy, XAS), short-to-medium range (total scattering/Pair Distribution Functions (PDF)), and long-range (PXRD) analyses, we evidenced the impact of both parameters (M and n) not only on the LT structures but also on the thermal properties and on the HT structures. For clarity, the results are organized according to temperature regimes: the synthesis and structure of the LT forms are described first, followed by the thermal transitions, and finally the structures of HT phases.

■ EXPERIMENTAL SECTION

Synthesis

$(C_nH_{2n+1}NH_3)_2MCl_4$ solids with M = Cu, Mn, Zn and n = 6, 7, 12, 13, 16 were prepared following previously reported procedures.[12,20,42,43] Alkylamine (≥99,0% purity), concentrated aqueous hydrochloric acid (37 wt %), and anhydrous copper, manganese, and zinc chloride were purchased from Sigma-Aldrich and used without further purification. The reactants are accurately weighed at the molar ratio of $C_nH_{2n+1}NH_2/HCl/MCl_2$ = 2:2:1.1 (the exact amount of reactants are summarized in Table S1). Amine was first dissolved in anhydrous ethanol with stirring at room temperature; aqueous hydrochloric acid was then added to the solution to ensure the complete protonation of the amine. After several minutes of stirring, MCl_2 was added to the solution and the solution was heated to reflux under stirring for 1 h. Crystals were obtained upon cooling the resulting solution to room temperature at a rate of 2 K min^{-1}. The crystals were recovered by filtration, washed with diethyl ether, and dried in air. Yield: 80 to 90%.

Characterization

DSC measurements of $\mathbf{C_nM}$ (n = 6, 12, 13, 16 and M = Cu, Zn, Mn) were conducted on a Setaram Calvet 3D instrument, while those of $\mathbf{C_7M}$ (M = Cu, Zn, Mn) were conducted on a TA Instruments Q20. Solids were ground, placed in a crucible, and subsequently heated at a rate of 1 K min^{-1} from 273 to 438 K and 220 to 438 K, respectively. Peaks associated with phase transitions were then fitted with Origin (OriginLab) using Gaussian (or Bigaussian depending on an asymmetry of peaks) multipeak fit after baseline subtraction. The onset and offset temperatures were then defined as the temperatures at which the specific heat flow (Q) reached 1% of the peak maximum value. The heat capacity (C_p) being the heat flow divided by the heating rate $\dot{T}$ and associated enthalpy as the integration of these peaks. Entropy curves were constructed by integrating the cumulative fit of C_p divided by T in accordance with

$$\Delta S(T) = \int_{T_0}^{T} \frac{1}{T}\frac{Q(T)}{\dot{T}}\mathrm{d}T$$

Temperature-dependent Fourier-transformed infrared (FTIR) spectra were recorded with a Bruker Vertex 70 spectrometer equipped with a diamond ATR heating plate. Data were collected between 400 and 4000 cm^{-1}. Temperature-dependent Raman spectra were recorded at a 633 nm (He−Ne laser) excitation either on a Renishaw InVia Reflex spectrometer equipped with a Bragg network in order to measure down to 20 cm^{-1} (n = 12, 13, 16) or with a Jobin-Yvon T64000 spectrometer (n = 6, 7). Both spectrometers were equipped with a Linkam heating−cooling stage to vary the temperature. SCXRD analyses of the as-prepared solids were performed at room temperature (except 200 K for $\mathbf{C_7Cu}$) using a Rigaku XtaLAB Synergy-S diffractometer equipped with a Mo Kα microsource (λ = 0.710747 Å) and a HyPix-6000HE detector. The CrysAlisPro suite was used to integrate and scale intensities, and a semiempirical absorption correction (ABSPACK) was applied based on multiple scans of equivalent reflections. The structures were solved by direct methods using SHELXS and refined with the full matrix least-squares routine SHELXL[44] using the OLEX package.[45] Non-H atoms were refined anisotropically, while hydrogen atoms were introduced geometrically and refined using a riding model (instructions AFIX 23, 137, and 137 for CH_2, CH_3, and NH_3 groups, respectively). Crystallographic details are summarized in Table S2. PXRD and total scattering experiments were conducted in the transmission mode using rotating capillaries to reduce the preferred orientation. The solids were gently ground in a mortar, sieved at 150 μm, and placed in 0.5 mm glass capillaries. Temperature-dependent high-resolution synchrotron PXRD experiments were conducted at the CRISTAL beamline of the Synchrotron SOLEIL (Saint-Aubin, France) by using a monochromatic X-ray beam (λ = 0.6713 Å) and a Dectris Mythen 1D detector. Whole structureless powder pattern fittings were conducted with JANA2006.[46] For the PXRD-based structure determination, indexation was carried out either with the DICVOL program[47] implemented in the FullProf suite[48] ($\mathbf{C_6Zn}$_HT) or with Topas[49] ($\mathbf{C_7Zn}$_INT, $\mathbf{C_{13}Zn}$_INT). In the three cases, the structure determination was performed by paralell tempering with the program FOX,[50] and final validation via Rietveld refinements were conducted using either JANA2006 or JANA2020.[46] For $\mathbf{C_6Zn}$_HT, the structure involved three $ZnCl_4$ groups (occupancies of 0.57, 0.27, and 0.17) and four cations $C_6H_{13}NH_3$ (occupancies of 0.5) and distance restraints. Crystallographic details are summarized in Table S3. CCDC-2497694 to 2497708 contain the supplementary crystallographic data for all of the reported structures . These data can be obtained free of charge from the Cambridge Crystallographic Data Centre at https://www.ccdc.cam.ac.uk/structures. Measurements combining PXRD, total scattering, and XAS were performed as a function of the temperature at the BM31 beamline at the European Synchrotron Radiation Facility (ESRF, Grenoble, France) using a cryostream from Oxford Instruments. Two-dimensional powder diffraction images were collected with a monochromatic X-ray beam (λ = 0.25448 Å and 0.25995 Å in powder diffraction and total scattering configurations, respectively) using a Dectris Pilatus X CdTe 2 M detector and subsequently

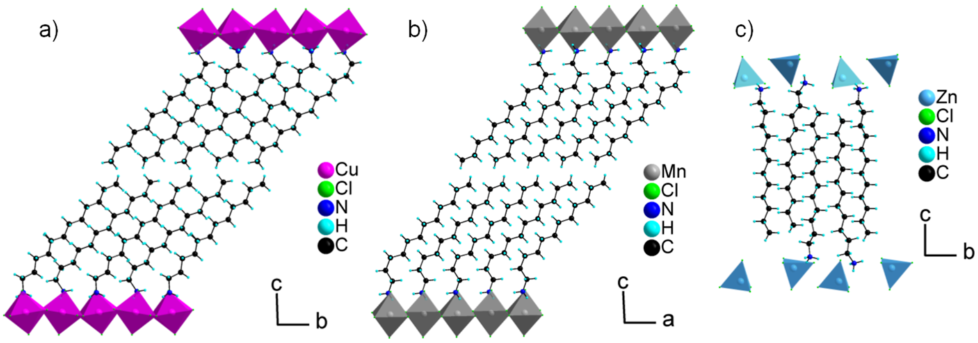

Figure 1. Room-temperature (LT) crystal structures of (a) $C_{12}Cu$, (b) $C_{12}Mn$, and (c) $C_{12}Zn$, highlighting the relative packing of the alkyl chains (chains facing each other for (a,b), interdigitated for (c)).

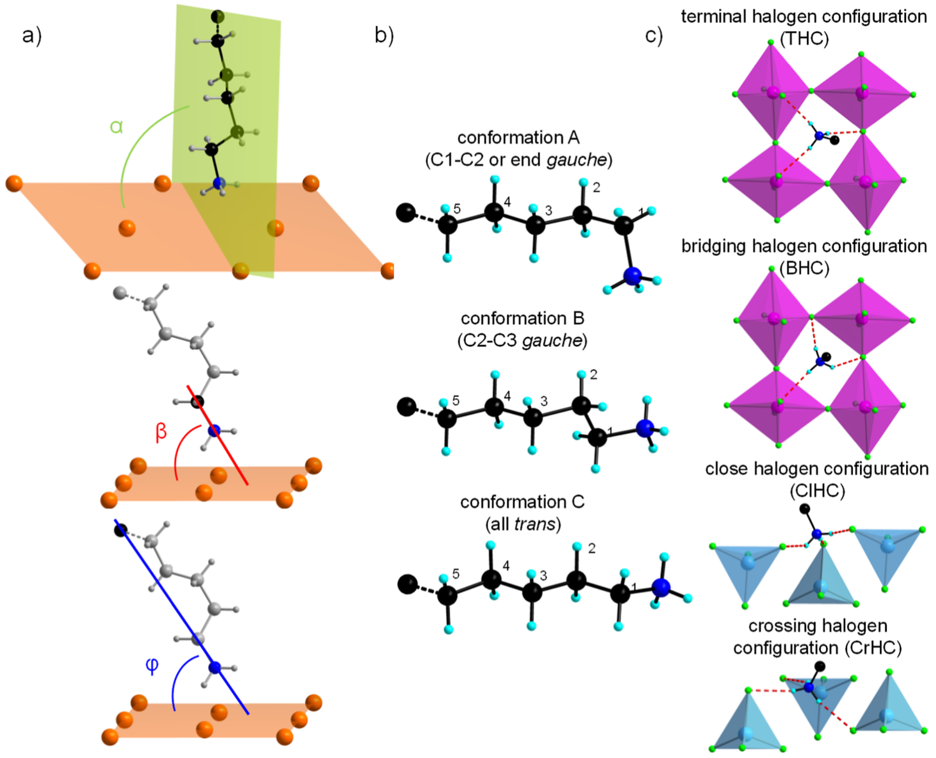

Figure 2. Local features in the LT crystal structures of C_nM. (a) Relative orientation of the alkylammonium chain and the inorganic layer; α = dihedral angle between the plane defined by all the non-H atoms of the alkylammonium chain and the plane defined by the metallic cations; β = angle between the N−C bond and the plane defined by the metallic cations; φ = angle between the vector connecting N and the last C atom of the chain and the plane defined by the metallic cations; (b) most common conformations of the alkyl chains; and (c) NH···Cl hydrogen bond configurations.

azimuthally integrated into 1D profiles with the SNBL Bubble client software.[51] For the PDF patterns, cosmic masking, integration and gain map were processed with the IMAGIN maskGenerator_CdTe code (https://github.com/msujas/maskGenerator_CdTe). XAS spectra were recorded in transmission making use of gas-filled ionization chambers at either the Cu 8979 eV or the Zn 9659 eV K-edge, using Cu and Zn reference foils for energy calibration. Extended X-ray Absorption Fine Structure (EXAFS) analysis was conducted using the DEMETER system.[52] Backscattering amplitude and phase were calculated using the FEFF10 code including self-consistent calculation of potentials to estimate the Fermi level.[53,54] Once EXAFS oscillations $\chi(k)$ were extracted with k(Å^{-1}) the photoelectron wavenumber, Fourier transformations of $k^2\chi(k)$ were taken on the largest possible k-range, typically [3.15; 14.15] Å^{-1} for Cu and [3.1; 13.5] Å^{-1} for Zn. EXAFS data were fitted using the structural model described in the main text with the addition of a second sphere of nitrogen atoms. The final parameters of the fits are summarized in Table S9.

■ RESULTS AND DISCUSSION

Low Temperature Forms

All 15 solids $(C_nH_{2n+1}NH_3)_2MCl_4$ (M = Cu, Mn, Zn and n = 6, 7, 12, 13, 16) were easily produced at the gram scale following the reported procedure. In line with their layered structures, they were isolated as large but thin crystalline platelets (typically larger than 100 × 100 μm^2 and thinner than 10 μm) but suitable for SCXRD analysis. Among the studied solids, the crystal structures of a few of them were already reported (see references in Table S8). The other ones were solved at room temperature (except 200 K for $\mathbf{C_7Cu}$), i.e., below the first phase transition, and for this reason later quoted LT forms.

The corresponding crystallographic parameters are summarized in Table S2. A structureless whole powder pattern fitting of the PXRD patterns further confirmed that the single-crystal structures are a representative of the bulk samples (Figures S1−S3). The compounds were also examined by IR spectroscopy; a thorough analysis can be found in the Supporting Information. The crystal structures obtained in the present work are in agreement with the already published ones and related compounds with very close chain lengths (see references in Table S8). For a given cation, similar structural arrangements are observed whatever the chain length *n*. As expected, Cu-based and Mn-based materials contain 2-D anionic perovskite sheets, while for the Zn-based materials, the anionic layers consist of isolated $ZnCl_4^{2-}$ tetrahedra. In both cases, these inorganic layers alternate with cationic organic bilayers made of parallel aliphatic chains interacting with each other through van der Waals interactions and with the anions through N−H···Cl hydrogen bonds. However, the arrangement of these bilayers differs: for Zn-based materials, the chains of the two constitutive layers are interdigitated, while for the Cu- and Mn-based materials, they are facing each other (Figure 1). This difference does not derive from the atomic arrangement of the inorganic layer, but rather from their relative charge density. The areal anionic charge density is indeed significantly lower in the Zn-based layer than in the Cu and Mn-based ones (one negative charge per ∼19 and ∼13 Å^2, respectively), leading to a less dense packing of the ammonium heads and hence interdigitation. Such an interdigitation can indeed be also found in 2-D perovskite type solids presenting longer M-X distances and hence low areal charge density such as those based on Pb and I (one negative charge per ∼19 Å^2).[23]

As mentioned above, both Cu- and Mn-based materials are built up from 2-D perovskite sheets, hence consisting of corner sharing [MCl_6] octahedra. The main difference between the Mn- and Cu-based solids arises from the Jahn−Teller distortion of the $CuCl_6$ octahedra that typically present four short (two equatorial and two terminal) and two long (equatorial) Cu−Cl distances of ∼2.3 and ∼2.9 Å, respectively (Table S4). This effect can be measured with the octahedral distortion parameter Δd that quantifies the deviation to the mean Cu−Cl distance.[55] Although a decrease of this parameter with the chain length, especially for the high value of *n*, is detected, the variation of this parameter is low (<10%, see Table S4 and Figure S4), confirming that the organic chain has a very limited impact on the geometrical features of the inorganic layer. 2-D perovskite structures can be described using symmetry mode analysis to identify the structural distortion of the $\{MCl_4^{2-}\}$ infinite sheets, as already done, e.g., for $\{PbI_4^{2-}\}$-based solids.[56,57] The main distortions observed in this family can be divided in two types: tilting of the octahedra and shifts of the inorganic layers from one layer to another (see Supporting Information and Table S5 for a complete discussion including the relationship between tilts, shifts, and space group assignment). Tilt systems of Cu-based and Mn-based materials are identical for all structures except **C_{16}Mn**, while the shift of the inorganic layer evolves with the length of the alkyl chain *n* as discussed below. In order to describe the direction of the organic chains vs the metallic mean plane, we used the 3 angles $\angle_\varphi$, $\angle_\alpha$, and $\angle_\beta$ introduced by Lemmerer and Billing *et al.* again for $\{PbI_4^{2-}\}$-based solids (Figure 2a).[23] φ and α relate to the average direction of the aliphatic chain, while β is the angle between the N−C bond and the inorganic layer and will be discussed below. Organic layers are composed of bilayers of tilted chains with similar $\angle_\varphi$ around 45° and $\angle_\alpha$ around 60° whatever the chain length (see Table S6). Consequently, the shift between the inorganic layers mentioned above depend on *n*, and their relative packing evolves between fully eclipsed, half staggered, and fully staggered (Dion Jacobson, Dion-Jacobson 2 (DJ2) and Ruddlesden−Popper configuration (RP), respectively, see Table S5). The organic chains adopt mainly two conformations independently on *n* and M: conformation A (or end-*gauche*), consisting of an all-*trans* alkyl chain except a gauche conformation along C1−C2 (C1 being the C atom linked to the ammonium head) and conformation B, consisting of an all-*trans* alkyl chain except a gauche conformation along C2−C3 (Figure 2b).[28] For Cu-based materials, especially those with *n* ≥ 12, half of the chains are disordered over two positions with two different conformations, B and fully all-*trans* (denoted conformation C, see Figure 2b). The ammonium groups occupy a "box-shaped" space defined by four terminal and four bridging chloride ions and are involved in three N−H···Cl hydrogen bonds. Although the precise position of the H atoms derived from SCXRD analysis should always be considered with care, as proposed by Mitzi, it is possible to define here two configurations:[1] a "terminal halogen configuration" (THC) involving N−H···Cl hydrogen bonds with two terminal chloride and one bridging chloride, and a "bridging halogen configuration" (BHC) with bridging chloride and one terminal chloride (Figure 2 and Table S7). Note that the presence of these two configurations was also supported by IR spectroscopy (Figure S8). The hydrogen bond configuration directly relates to angle β, with $\angle_\beta$ equal to ∼30 and ∼15° for THC and BHC, respectively (Table S6). Most of the ammonium ions adopt THC, and BHC is almost exclusively observed for chains adopting conformation C (see Table S8). This aligns well with the proposition of Rey-Lafon *et al.*,[58] who hypothesize that the coexistence of conformation C with so-called conformations A and B require either distortions of the octahedra or a hydrogen bond scheme other than THC. Both propositions seem to be correlated, as the association conformation C/BHC is found exclusively for structures made of Jahn−Teller distorted $CuCl_6$ octahedra. The evolution of the equivalent displacement parameter (U_{eq}) of the carbon atoms along the chain was also examined (Figures S5 and S6). Whatever the metal, the length of the chain *n* and its conformation, U_{eq}, continuously increases from C_1 to C_{n-2}, and further sharping increases for C_{n-1} and C_n (tail of the chain). This suggests a continuous evolution of the mobility of the C atom along the alkyl chain, from rather static close to the inorganic polar part of the framework to highly mobile in the apolar "hydrocarbon-rich" part, in line with the relative strength of the supramolecular interactions at play (strong and directional vs weak and nondirectional, respectively). A variation of the relative orientation of the organic layers with M and *n* was also observed (see Supporting Information and Figure S7), although it had a very limited impact on the thermal properties.

For the Zn-based materials, the inorganic layer consists of isolated $ZnCl_4$ tetrahedra arranged in a triangular lattice. Zn−Cl bond distances fall in the expected range (Table S4), and no disorder is detected in the LT forms. The position of the alkyl chains vs the inorganic layer was evaluated, again using the 3 angles described above (Table S6). The angles defining the main direction of the chains ($\angle_\alpha$ and $\angle_\varphi$) were found to depend on the parity: even organic chains are almost perpendicular to the inorganic layer with a $\angle_\alpha$ value of ~85° and exhibits a $\angle_\varphi$ tilt angle around 10°, whereas for odd chains these angles reach 78° and 18°, respectively. Such a difference has a direct impact on the thermal properties, as discussed in the next section. Contrary to what is found for the 2-D perovskites materials, the chain adopts almost systematically the all-*trans* conformation C (Table S8). Ammonium heads occupy cavities defined by $ZnCl_4$ tetrahedra and interact with chloride through hydrogen bonds (see Table S7 for the distances and angles). Considering that the inorganic layers consist of two sheets of chloride sandwiching one sheet of zinc, two configurations of the hydrogen bond can be defined, again in agreement with the IR analysis (Figure S8): the "close halogen configuration" (ClHC) and the "crossing halogen configuration" (CrHC), with the ammonium head interacting with three chlorides from the same (and closest) sheet, and with two chlorides from the closest sheet and one chloride from the farthest sheet, respectively (Figure 2c). The $\angle_\beta$ angle is again a characteristic of the hydrogen bond configuration, with $\angle_\beta$ angles ~45° and ~19° for ClHC and CrHC, respectively (Table S6). The evolution of the equivalent displacement parameter U_{eq} along the alkyl chain is shown in Figures S5 and S6. Although the averaged values of U_{eq} are only slightly higher than that found in 2-D perovskites materials, their evolution with n differs: U_{eq} indeed remains almost constant from C_1 to C_{n-2}, and it increases significantly only at the tail of the chain (C_{n-1} and C_n), but to a lesser extent. This likely comes from the interdigitation of the chain mentioned above, which prevents the formation of a very soft area in the structure, free of any strong and directional supramolecular interaction. Hence, the motion of the organic cation in the LT forms might be different in both series of materials: a static head with a dangling chain in the Cu- and Mn-based compounds vs possibly a more collective motion of the cation for the Zn-based materials.

Temperature Induced Phase Transitions

DSC was first used to determine the temperature of the phase transitions and the associated enthalpies for all $\mathbf{C_nM}$ materials. The DSC curves are shown in Figures 3 and S9, while the derived temperatures and enthalpies of transition are summarized in Figure 4a,b, respectively, together with the data available from the literature for the other members of the series.[7,25,59] While for all 2D-perovskite solids, but $\mathbf{C_{16}Cu}$, the first transition is the main one (i.e., associated with the highest enthalpy), the Zn-based solids all present secondary transitions of lower enthalpies both below and above the main one. Whatever the cation and structure type, the number of phase transition seems to broadly increase with the length of the organic chain and does not correlate neither with the symmetry and size of the asymmetric unit of the LT structures nor with the tilting scheme of the MCl_6 octahedra for the 2-D perovskite structures (see the Supporting Information). For the materials based on long-chain ammoniums (typically $n \geq 9$) whatever the structure type and metallic cation, both the temperature and enthalpy of transition evolve roughly linearly with n. For those based on short-chain ammonium ($n \leq 7$), although the enthalpies seem to follow the same trend, the temperatures of the main transition are highly dispersed and do not seem to follow a specific trend (Figure 4a, gray zone). Moreover, whereas both 2-D perovskite materials behave similarly for long-chain ammoniums, the temperature of the transition differs for short-chain ammoniums for M = Cu and Mn. This suggests that while organic–organic interactions govern the phase transitions for the high values of n, organic–inorganic interactions, or purely inorganic phenomena, might play also a significant role for the low values of n. Note that a

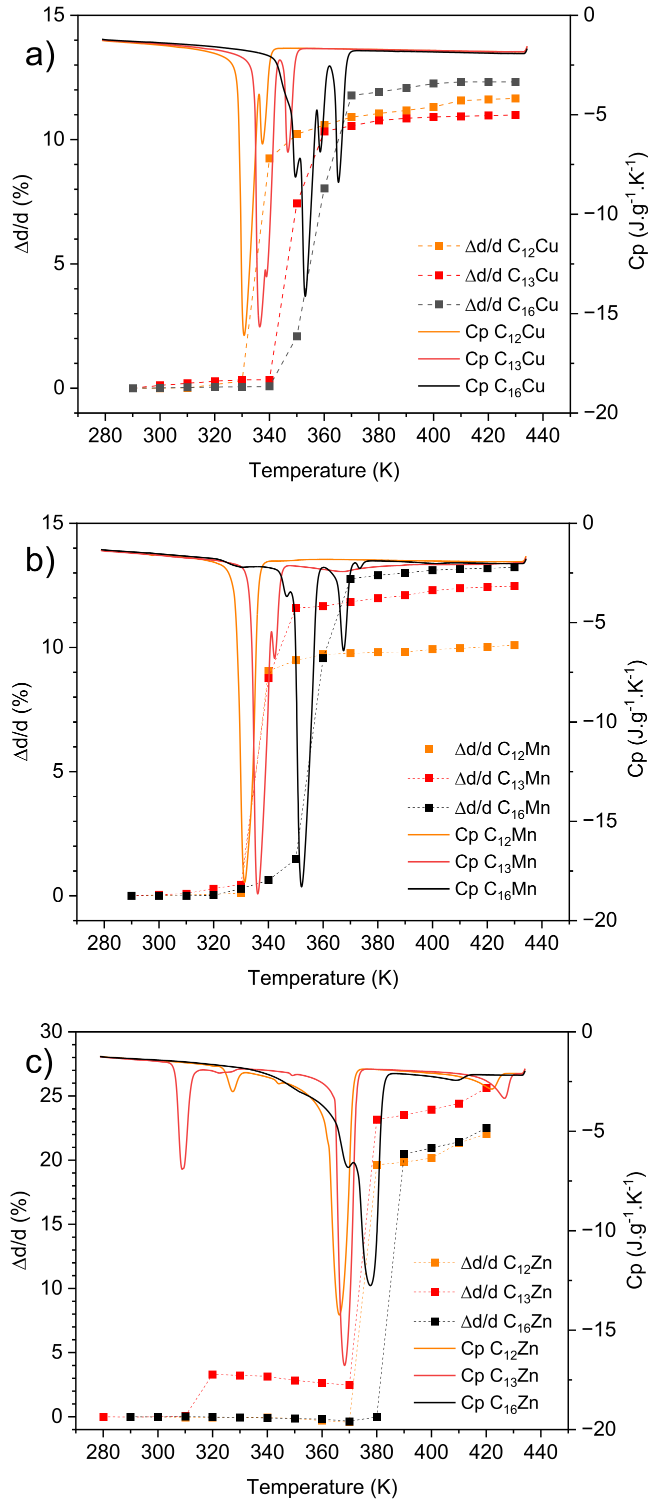

Figure 3. DSC curves (plain lines) of the C_nM materials (n = 12, 13, 16) obtained upon heating at 1 K min^{-1} under static air in a closed crucible (see Figure S9 for n = 6, 7). The relative variation of the interlayer distances $\Delta d/d$ estimated from the fit of the first 00*l* Bragg peaks on the T-dependent PXRD is also shown (dashed lines).

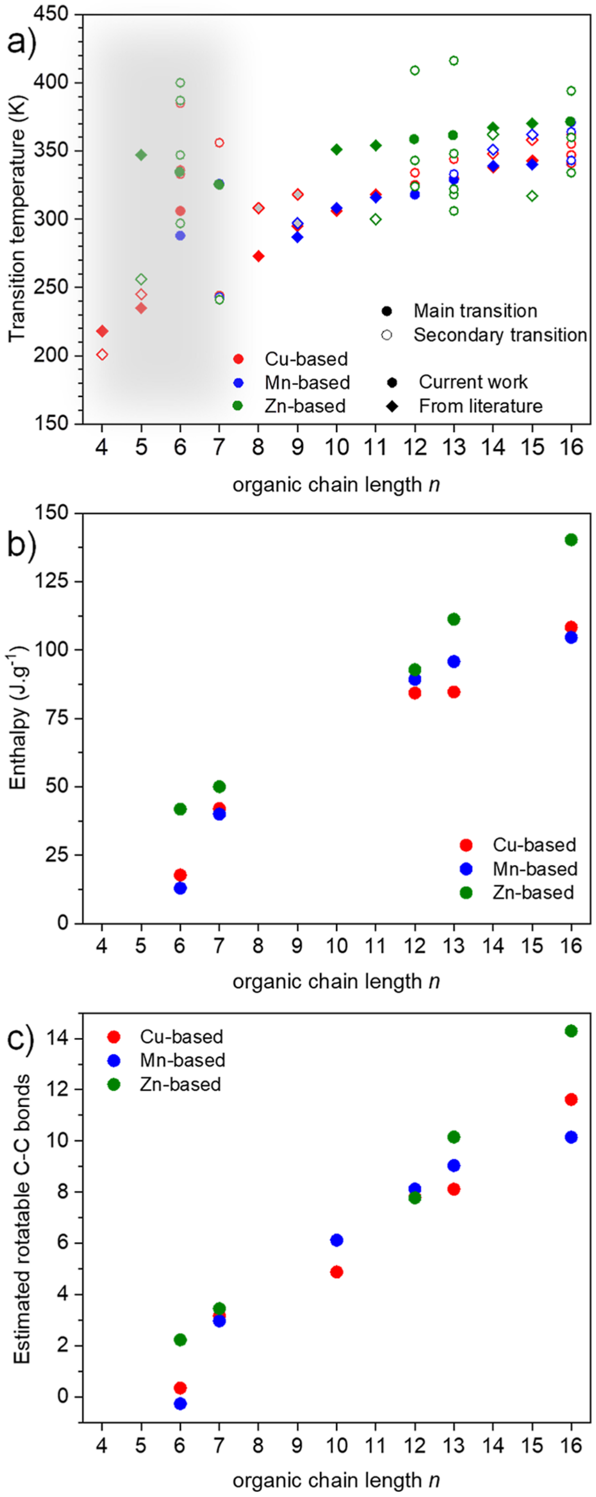

Figure 4. (a) Temperature and (b) cumulative enthalpy of transition extracted from the DSC analyses. For (a), data available in the literature for C$_n$Cu (n = 4, 5, 8[25] and n = 9, 10, 11, 14, 15[7]), C$_n$Mn (n = 9, 10, 11, 14, 15),[7] and C$_n$Zn (n = 5, 10, 11, 14, 15)[59] are also shown. (c) Number of newly rotatable C−C bonds in the HT form estimated from the entropy curves derived from the DSC analysis (see Figure S10).

similar chain length dependency was found by Schenk and Chapuis for the 2-D perovskite **C$_n$Cd** materials.[27] For a given chain length, both the temperature and enthalpies of the main transition are systematically higher for the Zn-based materials than for the 2-D perovskites, while, as mentioned above, at least the enthalpies are the same for M = Cu and Mn. It was reported that the main transitions involve a modification of the conformation of the alkyl chains and of their packing.[28,29,31] As discussed above, both features are different in the initial LT forms of 2-D perovskite and non-perovskite materials and could be at the origin of such a discrepancy. The fact that the C$_n$PbI$_4$ (n = 7−10) solids that consist of 2-D perovskite layers with alkyl chains in conformations A and B (similar to Cu- and Mn-based materials), but interdigitated, present temperatures of transition similar to that of the Zn-based solids[23] suggests that the packing effect is predominant. Interdigitation indeed imposes a close proximity of the static (ammonium head) and mobile (alkyl tail) parts of the organic cations[41] that might hinder their motions when compared to the other structural arrangements, where all the mobile parts are close together. Eventually, for the Zn-based materials, a clear effect of the parity of the organic chain is observed, with secondary transitions observed at lower temperatures for odd chains when compared to even chains (Figure 4a) and likely relates the different orientations of the chains relative to the inorganic layer for even and odd numbers of carbon atoms (see above).

The entropy of all transitions was deduced from the enthalpy, and, assuming order−disorder transitions, used to further estimate the number of rotatable C−C bonds appearing during each transition.[5,12] The resulting data are shown in Figures S10 and 4c, respectively. For the Zn-based materials, the entropy appears to be proportional to the organic chain length whatever the value of n, whereas for the 2-D perovskite materials, the evolution differs for short and long chains. For $n \geq 12$, the evolution is similar to that observed for Zn-based solids, while for n = 6, the variation of the entropy is very low. This suggests that no new rotatable C−C appear for short organic chain 2-D perovskite materials and that they do not undergo order−disorder transition. Long-chain 2-D perovskite materials as well as all Zn-based materials undergo order−disorder transitions with consistent values of newly rotatable C−C bonds (∼n − 3 and ∼n − 4 bonds for M = Zn, and M = Cu, Mn, respectively). Although more data points (especially for an intermediate value of n) will be needed to strengthen this conclusion, this analysis aligns well with the variation of the temperature of transition, which evidenced the distinction between short- and long-chain ammoniums for 2-D perovskite materials.

The solids were further analyzed by temperature-dependent synchrotron PXRD; the resulting data are shown in Figure 5 for the representative materials **C$_n$Cu** and **C$_n$Zn**, n = 6 and 12 (see Figures S11−S13 for other solids). While the structures of the intermediate and HT phases will be discussed later, a qualitative analysis can be drawn by considering the DSC results. In agreement with the literature on related materials, the phase transitions correspond to crystal-to-crystal transitions. Remarkably, even when the DSC curves are complex, all the events are detected by PXRD (for example 3 phase transitions identified between 330 and 345 K for **C$_{12}$Cu**, see Figure 5b). The phase transitions are associated with a shift of the main diffraction peaks 00l associated with the increase of the interlayer distance; when multiple transitions are present, the main transition is associated with the highest increase of this distance, while the variations are more limited for secondary transitions (see, e.g., **C$_{13}$M**, M = Cu, Zn in Figures S11 and S13). When considering the extreme forms (LT and HT), the interlayer distance increases by roughly 20% for Zn-

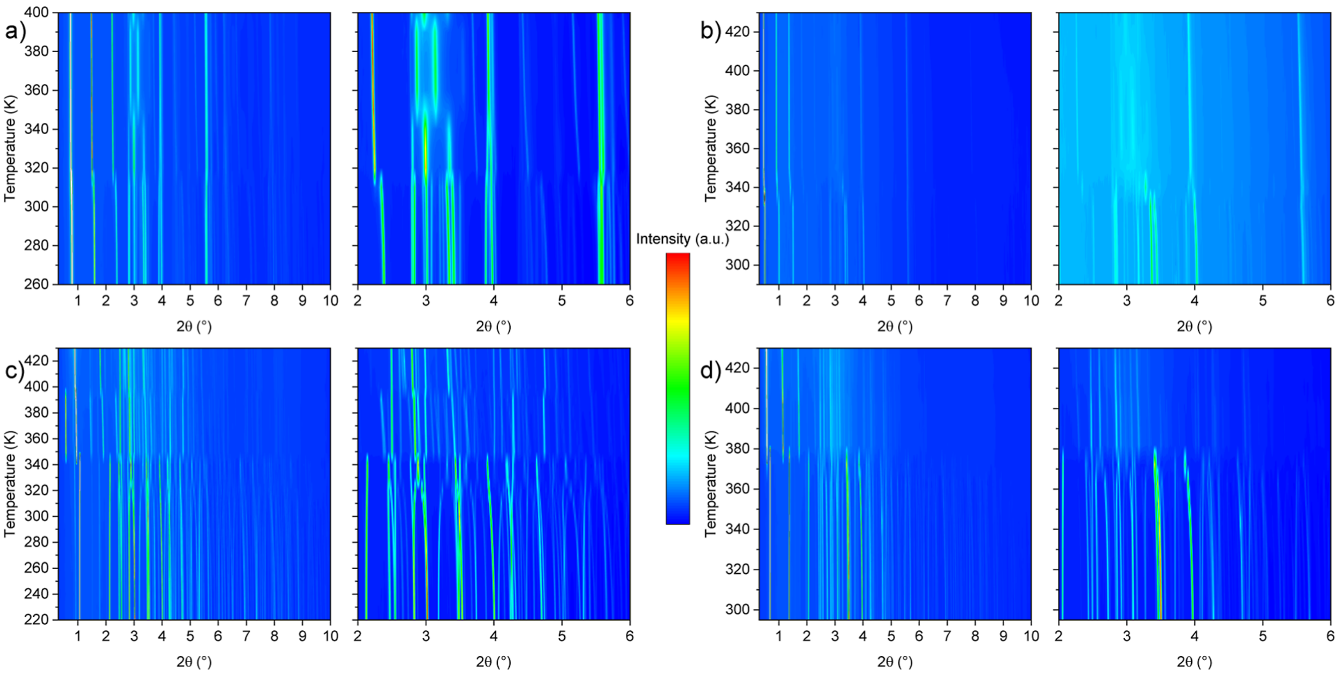

Figure 5. Temperature-dependent PXRD patterns of (a) C_6Cu, (b) $C_{12}Cu$, (c) C_6Zn, and (d) $C_{12}Zn$. Left: general view; right: zoom of the 2–6° region. $\lambda = 0.25448$ Å.

based materials while the increase is smaller for 2-D perovskite materials, below 10% and around 15% for the short and long alkyl chains, respectively (Figure 3). For Zn-based materials, weak diffraction peaks at Q values lower than the main $00l$ diffraction peak are observed for few intermediate phases and are likely indicative of superstructures (in the range 343–400, 334–360, 349–375, and 349–386 K, for n = 6, 7, 13, and 16, respectively). For the HT forms, these features disappear and well-defined symmetrical peaks even at high angles are observed, suggesting that a long-range order is maintained. The behavior of 2-D perovskite materials is different: in the HT forms, peak profiles are characterized by a strong asymmetry on the right, a characteristic of stacking fault defects commonly found in layered materials leading to the sawtooth-shaped cluster of peaks.[60] The phase transitions are also accompanied by an important increase in diffuse scattering (Figures S14–S16). This diffuse scattering is associated with disorder in the HT forms, likely of dynamic origin considering the quick damping of Bragg's peaks when $\sin(\theta)/\lambda$ increases that can be associated with huge thermal displacement parameters. This increase of diffuse scattering is qualitatively more marked for Zn-based materials than for 2-D perovskite materials (see Figures S14 and S15 vs S16), suggesting a more pronounced dynamic disorder. The increase is also much smaller for short organic chain materials, indicating similarly that disorder is more important for long organic chain materials. Hence, both DSC and T-dependent PXRD evidenced clear differences between Zn-, Cu-, and Mn-based materials on one side and short- and long-chain alkylammoniums on the other side, notably for 2-D perovskite-type solids. The following section is dedicated to understanding such differences through the study of the structures of the intermediate and HT forms.

Structures of the Intermediate and HT Phases

The structures of the solids after the transition(s) were studied by several techniques, with the aim at accessing (i) long-range (XRD), (ii) short-range (infrared, Raman, and XAS spectroscopies for the organic and inorganic parts, respectively), and (iii) short and medium range (PDF) information, notably through a single temperature-dependent synchrotron experiment combining XAS, PDF, and PXRD analyses (BM31, ESRF, France).

As mentioned in the introduction, solving the crystal structure of other forms than the LT for such a family of materials from XRD is challenging.[11,12,20−26] The strong noninstrumental asymmetry on the right of the diffraction peaks for the long-chain Cu- and Mn-based materials prevented the determination of the unit–cell parameters and further structure determination. Although intermediate phases with modulated structures have been reported for 2-D perovskites based on small organic cations,[25,61] no satellite diffraction peaks indicative of modulated structure was observed for all studied Cu- and Mn-based materials. Using single-crystal XRD, it was eventually possible to solve and refine the structure of one intermediate phase for a short-chain Cu-based solid, namely **C_7Cu** at 280 K. For the Zn-based materials, three structures were obtained thanks to high-resolution synchrotron PXRD: the intermediate forms of **C_7Zn** at 280 K and of **$C_{13}Zn$** at 340 K (quoted phase II in ref 21) and the HT form of **C_6Zn** at 423 K (see Table S3 and Figure S17 for the final Rietveld plots). Whatever the composition, the structures evolve on heating toward more symmetrical crystal systems (from triclinic to monoclinic, for **C_7Cu**, and monoclinic to orthorhombic for **C_nZn**, n = 6, 7, 13) in agreement with previous reports on homologous materials. The unit–cell parameters related to the inorganic layers remain almost constant, while the interlayer distance increases, as mentioned above (see Tables S1 and S2). When compared to the LT forms, the most noticeable modifications are as follows:

- For the intermediate form of **C_7Cu**, a slight modification of the tilt scheme of the $CuCl_6$ octahedra is observed

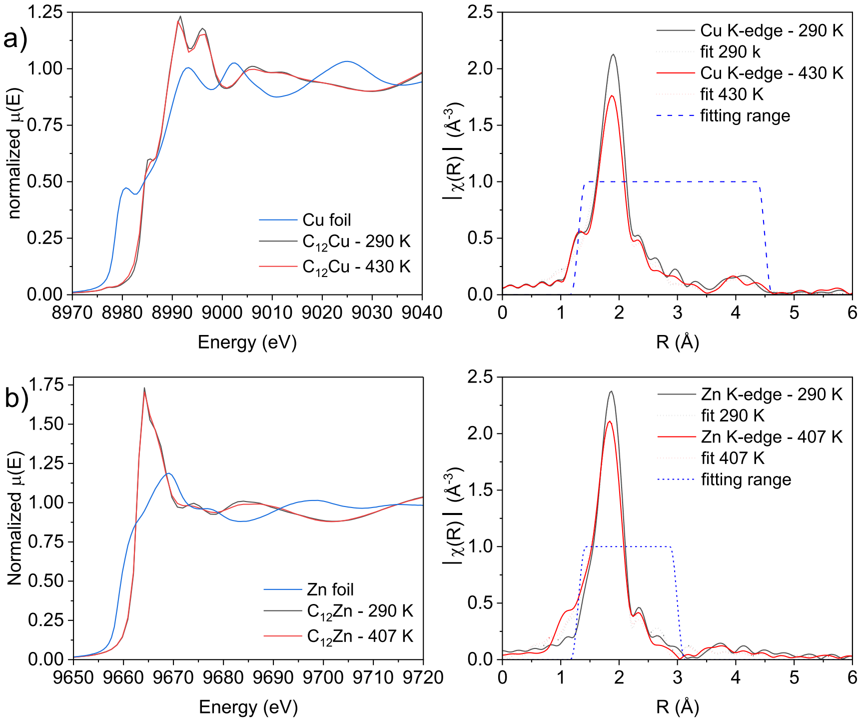

Figure 6. Metal K-edge XANES spectra (left) and EXAFS spectra (right) uncorrected for the phase shift for the (a) $C_{12}Cu$ and (b) $C_{12}Zn$ both in the LT (290 K) and HT (430/407 K) forms. For the XANES part, the corresponding reference metal foils are also shown; for the EXAFS part, the best fit is also plotted (see Table S9 for the fit parameters).

(Table S5). Regarding the organic moieties, the conformation of the alkyl chains evolves from A and B in the LT form to B and *gauche-gauche-trans-gauche-trans*, possibly coming from the introduction of a sort of kink in the cation presenting initially conformation A. No elongation of the N···Cl distances was detected for the cation adopting conformation B, while these distances significantly increase for the other one, potentially linking the introduction of a kink along the alkyl chain to the weakening of the N-H ···Cl hydrogen bonds. As found in the LT form, the equivalent atomic displacement increases monotonously when moving from the ammonium head to the tail of the alkyl chain, but the variation is far higher, suggesting a more pronounced thermal motion (Figures S5 and S6).

- For the intermediate forms of $\mathbf{C_7Zn}$ and $\mathbf{C_{13}Zn}$, the conformation of the alkyl chains remains similar to that of the LT forms (see Table S8), but their arrangement relative to the inorganic layer evolves, with the $\angle_\varphi$ tilt angle being close to 10°, a value similar to that found in the LT form $\mathbf{C}_n\mathbf{Zn}$ materials with even *n*. The number of short (<3.4 Å) Cl···N distances decreases, indicative of a potential weakening of the hydrogen bonds (Table S7).
- For the HT form of $\mathbf{C_6Zn}$, although still assembled into layers, the $ZnCl_4$ anions are statistically disordered over 3 positions with respective occupancies of 0.56, 0.27, and 0.17. The alkylammonium cations are disordered over at least two positions with a ∼0.5:0.5 occupancy and do not exhibit anymore a full-*trans* conformation.

Although complete structural models could be satisfactory refined, a strong disorder of the alkyl chains was detected in these structures, as expected.[12,21−26] The final refined atomic positions, especially those of the tail of the alkyl chains, should then be considered with caution; these models were then supported by the data issued from other analytical tools that probe the short (XAS, IR, Raman, and PDF) and medium range (PDF) distances, as discussed below.

In situ temperature-dependent XAS experiments at either the Cu or Zn K-edge were conducted simultaneously with the PXRD and PDF analyses; data for representative $\mathbf{C_{12}Cu}$ and $\mathbf{C_{12}Zn}$ in the LT and HT (430 K) forms are discussed below. First, the X-ray Absorption Near-Edge Spectroscopy (XANES) offers the possibility to assess the charge state of the metallic cations (Figure 6, left) using the variation of the energy of the edge. Here, the offsets relative to the reference metal foils are in agreement with II+ oxidation states for both Cu[62] and Zn,[63] both in the LT and HT forms, confirming that no redox process occurs during the phase transitions. The Extended X-ray Absorption Fine Structure (EXAFS) spectra representing the oscillation magnitude as a function of pseudo distance R are shown in Figure 6, right (see Figure S18 for the data as a function of the wavenumber). The position of the main contribution is rather constant and located at pseudo distances R = 1.88 and 1.86 Å for Cu- and Zn-based materials, respectively, with a small secondary contribution pointing around 4.2 Å for Cu. This indicates that the local structure around both Cu and Zn is mainly constituted by a single shell, while the shape of the envelope of the oscillations in k space shows that this shell is solely constituted by chloride ions (Figure S18). First fitting of the Cu environment in $\mathbf{C_{12}Cu}$ conducted using the SCXRD model (i.e., an octahedral environment with four chloride ions at 2.29 Å and two at 2.98 Å) led to a fair agreement. Both in the LT and HT forms, a better fit was indeed obtained using a first shell consisting of four chloride ions at 2.29 Å, one at 2.84 Å, and one a 3.02 Å (Figure S19 and Table S9). This suggests a slightly distorted octahedral environment for the Cu ion associated with a 0.1 Å displacement from the center of the Cl_6 octahedron along the

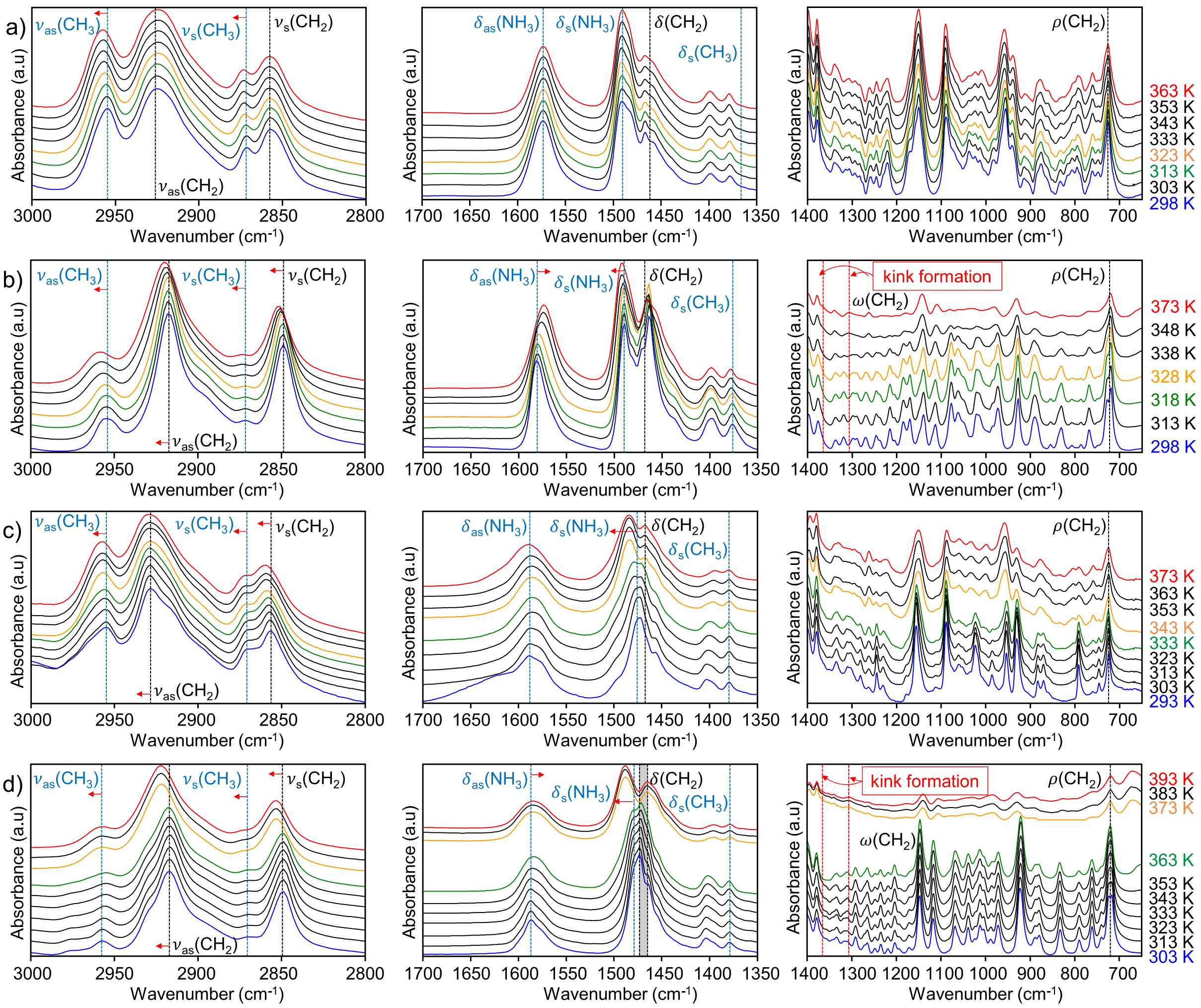

Figure 7. Temperature-dependent infrared spectra for (a) C_6Cu, (b) $C_{12}Cu$, (c) C_6Zn, and (d) $C_{12}Zn$ materials.

long Cu−Cl axis, not detected by XRD. It should be noted that no evolution of the environment of Cu was observed upon heating, in contrast with recent findings on a meltable lead bromide 2-D perovskite, for which a decrease of the coordination number was evidenced in the liquid state.[64] For $\mathbf{C_{12}Zn}$, a good quality fit is obtained with a first shell constituted by four chloride ions with a single Zn−Cl distance of 2.27 Å, compatible with the tetrahedral environment identified by SCXRD. This remains true both in the LT and HT forms (Figure 6b and Table S9). The XAS experiments thus confirmed that neither the oxidation state nor the first coordination shell of the metallic cations is impacted by the phase transitions.

Temperature-dependent infrared and Raman spectroscopies were used to monitor the evolution of the organic and inorganic moieties, respectively.[11,29,31−33,35] Cu- and Mn-based materials presented similar features; data for $\mathbf{C_6Cu}$ and $\mathbf{C_{12}Cu}$ are shown in Figure 7a,b, respectively. Vibrational characteristics of the CH_3 end groups evolve similarly, whatever the chain length. An increase of the wavenumber of the symmetric and antisymmetric $\upsilon(CH_3)$ bands from 2871 to 2874 cm^{-1} and from 2955 to 2958 cm^{-1} is observed on heating, indicating a modification of the environment of the tail of the alkyl chains. On the other hand, the evolution of the C−H stretching vibrations that are characteristic of the entire alkyl chain was found to depend on the chain length: for the high value of n (≥12), a shift of ~3 cm^{-1} toward higher wavenumbers of the CH_2 symmetric stretching bands is observed as well as a decrease of the gap between the two signals of the CH_2 bending and rocking band doublets. These evolutions are a characteristic of an increase of conformational disorder.[28,30,32,34,36,65] The appearance of CH_2 wagging bands at 1367 and 1310 cm^{-1} above the phase transition also unambiguously indicates the formation of kinks[66] and is not observed for short organic chain materials. This agrees well with the DSC analysis that indicated the appearance of rotatable C−C bonds only in the long-chain materials. No significant modification of NH_3 bending modes is also observed for short organic chain materials, while a broadening and shift of NH_3 symmetric and antisymmetric bending bands are observed for long organic chain materials, indicative of a weakening of the NH···Cl hydrogen bonds.[36] The frequency of these modes becomes identical to that of the short organic chain materials, suggesting that a single configuration of the hydrogen bond, namely, THC, remains in the HT form whatever the chain length. The Raman spectra were measured in the low-frequency region (100−300 cm^{-1}) to probe the vibration modes associated with the inorganic anions (Figure S20). For the Cu-based solids, three distinct vibrations are visible, all assigned to Cu−Cl stretching vibrations.[67−70] As shown in Figure S20 and Table S10, upon heating, the bands attributed to equatorial and terminal Cu−Cl symmetric

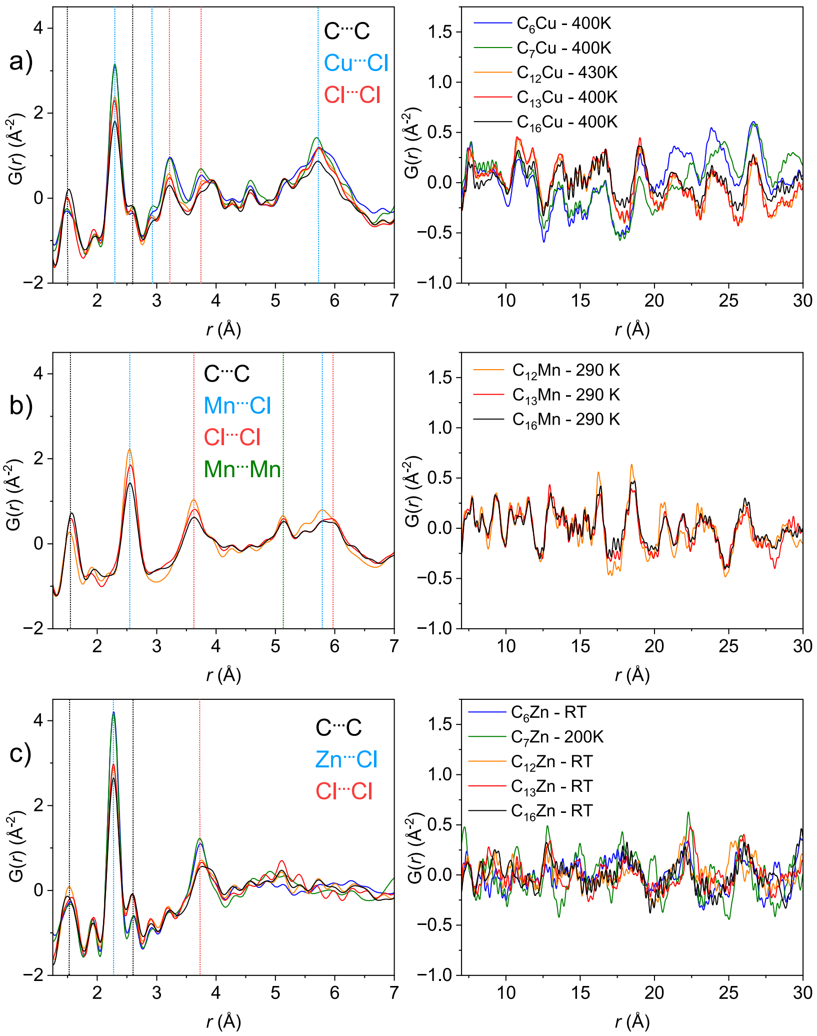

Figure 8. Reduced PDF for (a) C_nCu, (b) C_nMn, and (c) C_nZn in the LT forms, both at low (left) and medium (right) r values. PDF peaks were assigned based on the knowledge of the LT crystal structures (see Figure S21).

stretching modes are significantly red-shifted (6 to 8 cm^{-1}), while the other bands are less impacted (~2 cm^{-1} red shift). These shifts indicate a slight modification of the inorganic layer and are in complete agreement with the structure of the intermediate form of **C_7Cu**, in which a decrease of the tilt of the $CuCl_6$ octahedra was evidenced (see above). The fact that a similar shift is observed for other values of n (Figure S20) suggests that such a structural modification occurs in all 2-D perovskite materials, simultaneously with the modification of the conformation of the alkyl chains for the high values of n. For the Zn-based materials (Figure 7c,d), the band characteristics of the CH_3 groups (ν_s, ν_{as}, δ_s) evolve to reach the same values in the HT state whatever the chain length. A shift toward a higher wavenumber (~3 cm^{-1}) of the CH_2 symmetric stretching bands is also observed, indicative of an increase of the conformational disorder as found in 2-D perovskite materials, but in this case whatever the value of n. A broadening and shift of the NH_3 bending bands, indicative of a weakening of the NH···Cl hydrogen bonds, are also observed. This last result is consistent with the structures of the intermediate forms of **C_7Zn** and **$C_{13}Zn$**, for which a decrease in the number of N···Cl short contacts was evidenced (see above). On the Raman spectra, a single band at ~280 cm^{-1} attributed to the Zn−Cl stretching vibration is observed (Figure S20).[71] Whatever the chain length, these bands broaden and are shifted toward lower wavenumbers at high temperatures. Considering that the $ZnCl_4$ anions are maintained during the transitions, as confirmed by the EXAFS analysis, this suggests a modification of the surrounding of the anions at high temperatures in all **C_nZn** materials, which is in agreement with the crystal structures of the intermediate forms of **C_7Zn** and **$C_{13}Zn$**.

To summarize, vibration spectroscopies evidenced that the modification of the conformation of the alkyl chains during the phase transitions are associated with a very moderate variation of the geometry of the inorganic moieties and a weakening of the NH···Cl hydrogen bonds. It also confirms that while Zn-based materials behave similarly for all alkyl chain lengths, the behavior of 2-D perovskite materials depends on n, with the appearance of a strong disorder and kink sequences only for the long-chain materials.

PDF analyses, which allow probing both the short and medium range orders, were conducted. To the best of your knowledge, although well suited for the study of phase transitions involving different kinds of disorder,[72,73] this technique was only very recently applied to the study of the lamellar hybrid solids.[64] Because of the complexity of their structures (low symmetry, large and highly anisotropic unit-

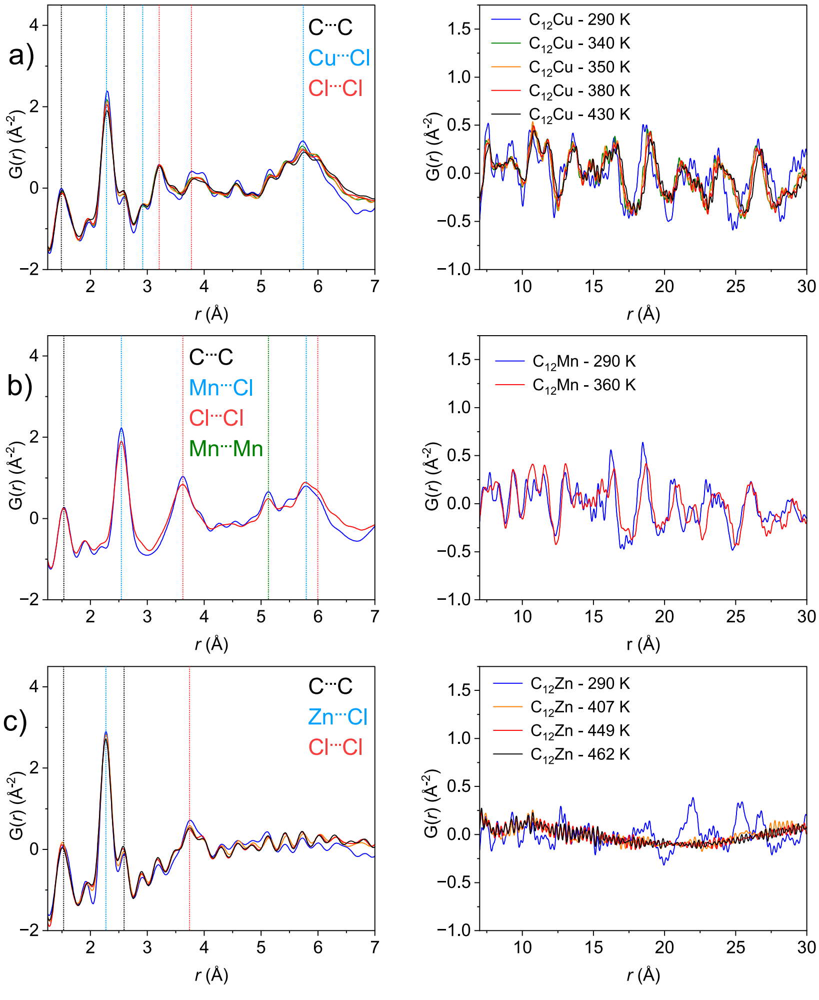

Figure 9. Temperature-dependent reduced PDF for (a) $C_{12}Cu$, (b) $C_{12}Mn$, and (c) $C_{12}Zn$ materials.

cell, and large number of independent atoms of various atomic number), it was not possible to quantitatively exploit the PDF data, such as refining the structures, notably in the INT and HT forms. Nevertheless, a qualitative analysis allowed identifying general features and assessing the relationship between the composition, the structure, and the thermal behavior of those solid−solid phase change-layered hybrid materials, as detailed below. Figure 8 presents the PDF of the LT form of all of the $\mathbf{C}_n\mathbf{M}$ solids. The PDF traces can be divided into two regions, the short-range ($r < 7$ Å), and the medium-to-long-range ($7 < r < 30$ Å). In the short-range domain (Figure 8, left), the peaks were identified through PDF simulations based on the knowledge of the LT crystal structures (Figures S21). As expected, this area is dominated by interatomic distances involving the heaviest atoms, namely M···Cl and Cl···Cl. Weaker peak characteristics of C−C bonds and C···C distances at 1.5 and 2.5 Å are also visible, while unfortunately C···C distances associated with specific conformations (e.g., ∼3.15 and ∼3.9 Å for *gauche* and *trans* conformations, respectively) are not detected. The position of the peaks is thus identical within a $\mathbf{C}_n\mathbf{M}$ series but differs for M = Cu, Mn, and Zn. For the Cu-based solids, five main peaks are visible below 7 Å (Figure 8a, left). The ones at 2.3 and ∼2.9 Å are associated with Cu−Cl bonds, in line with the Jahn−Teller distortion (see above), while the ones at 3.2 and 3.7 Å correspond to intraoctahedra Cl···Cl distances. The peak at ∼5.8 Å is associated with Cu···Cl distances within the inorganic layer and is a characteristic of the perovskite arrangement. The relative intensities of these peaks decrease when *n* increases. This is in full agreement with the evolution of the relative weight of the inorganic and organic fragments within the $\mathbf{C}_n\mathbf{Cu}$ series. For the $\mathbf{C}_n\mathbf{Mn}$ series (Figure 8b, left), the analysis is similar, with peaks at 1.5, 2.5, and 3.7 Å associated with C−C, Mn−Cl, and Cl···Cl distances, respectively, and peaks at 5.2 and ∼5.8 Å corresponding to Mn···Mn and Cl···Cl/Mn···Cl distances and characteristics of the perovskite layers. Regarding the medium range distance (Figure 8a,b, right), all $\mathbf{C}_n\mathbf{Cu}$ and $\mathbf{C}_n\mathbf{Mn}$ compounds present well-defined peaks indicative of ordered materials, but the PDF traces depend on *n*. While the short length materials ($n = 6, 7$) have specific patterns, the ones of the long-chain materials ($n = 12, 13, 16$) are identical and dominated by contributions exclusively related to the inorganic part of the structure (Figure S22). Considering that the amount of the organic moieties within the material is higher for the high values of *n* (in agreement with the analysis of the short-range domain), the fact that almost no signal related to the organic chains is visible at the medium range indicates that the long chains are poorly ordered at this scale even in the LT forms, while more ordered for the low values of *n* (6, 7). For Zn-based materials, in the low *r* region, three main peaks at 1.5, 2.2, and 3.7 Å are visible, corresponding to C−C bonds, Zn−Cl bonds, and both intra- and intermolecular Cl···Cl distances, respectively. Again, the relative intensity of the two peaks associated with the inorganic anions decreases when *n* increases, while, at the same time, the peak at 2.6 Å, a characteristic of C···C distances (see Figure S21) increases (Figure 8c, left), in agreement with the variation of the chemical composition. In the medium range, defined peaks indicative of ordered materials are present, but their position seems to depend more on the chain length than for the 2-D perovskites. It also appears clearly that the damping of the peak intensity as *r* increases is more pronounced for all the Zn-based materials with regard to the Cu- and Mn-based ones, as evidenced by poorly structured and noisy PDFs above 7 Å. This could be related to the higher values of theU_{eq} of the inorganic moieties in the Zn-based materials that suggest a less ordered state, even in the LT forms.

Temperature-dependent PDFs for **$C_{12}M$** (M = Cu, Mn, Zn) materials are shown in Figure 9 (see Figures S23−S25 for other alkyl chain lengths), both at low and medium *r* distances. For the Cu- and Mn-based solids, in the low *r* region, the variation is very moderate whatever the chain length *n* and state (INT and HT). The peaks corresponding to the Cu−Cl bonds at 2.3 and 2.9 Å remain, as well as those at 3.3 and 3.7 Å, a characteristic of the intra- and interoctahedra Cl···Cl distances, and the one at 5.8 Å corresponding to Cu···Cl distances. The same is true for the Mn-based materials, with characteristic peaks at 1.5, 2.5, 3.7, 5.2, and ∼5.8 Å, associated with C−C, Mn−Cl, Cl···Cl, Mn···Mn, and Cl···Cl/Mn···Cl distances, respectively. This indicates that at the short-range distance, the perovskite layers are not significantly affected by the transitions. In the medium *r* range, the solids present a signal characteristic of ordered materials even above the main phase transition (i.e., in the HT form), and this whatever the chain length (Figures S23−S25). This suggests that the stacking faults detected by PXRD for a high value of *n* do not significantly disrupt the order at this scale. Interestingly, all **C_nCu** solids even show a remarkably similar PDF signal in the HT phases (Figure S26a), the same is true for the **C_nMn** series (Figures S24 and S26b). This clearly confirms that the perovskite layers are maintained at a medium range. Peaks not associated with the inorganic layer are still detected for the short-chain materials (*n* = 6, 7), indicating that a certain degree of order of the organic cation is maintained in these solids. For the Zn-based materials (Figures 8c and S25), the evolution is markedly different. In the low *r* domain, the peaks at 1.5, 2.2, 2.5, and 3.7 Å associated with C−C, Zn−Cl, C···C, and Cl···Cl distances, respectively, remain visible both in the INT and HT forms, whatever the chain length. In the medium range, while in the INT forms, peaks indicative of ordering are maintained, almost no peak is visible above the main phase transition (i.e., in the HT form), suggesting a quasi-amorphous state, again whatever the chain length. This is at first sight very surprising given that the corresponding PXRD patterns present very well-defined diffraction peaks (Figure S16), but this is in agreement with the massive diffuse scattering found in the HT forms. Note that such a peculiar feature was already observed in purely inorganic salts containing tetrahedral units such as the HT form of the ion conductor Na_3PS_4, and described as freely rotating PS_4 units in a liquid-like environment.[74] Here, considering that the $ZnCl_4^{2-}$ anion is also maintained as evidenced by Raman spectroscopy and XAS, this indicates a drastic loss of order in the inorganic layer. This is in full agreement with the crystal structure of the HT form of **C_6Zn**, in which a strong positional disorder of the $ZnCl_4$ anion was detected, associated with the statistical occupancy of different disordered sites for Zn (see above). This further indicates that although Zn-based materials and Cu- and Mn- based 2-D perovskites share many common features and have closely related structures in their LT forms, their HT structures are of very different natures.

Considering these results and those extracted from the spectroscopic and diffraction analyses, we could qualitatively describe the structure of the HT states as follows:

- Independently of the value of *n*, **C_nZn** materials likely consist of dynamically disordered (IR and DSC) alkyl ammoniums weakly hydrogen bonded (IR) to intact (Raman, XAS), but statistically disordered, $ZnCl_4$ anions still located in the same average layer (XRD), but with no directional order between the $ZnCl_4(cation)_2$ triads (PDF).
- Oppositely, for **C_nCu** and **C_nMn** materials, the long-range order of the inorganic layer is maintained (XRD, PDF), although with a reduction of the tilt of the MCl_6 octahedra (XRD, Raman). The inorganic layers interact through weaker hydrogen bonds with the ammonium heads (IR), and only the long-chain materials present a massive conformational disorder of the alkyl chains (DSC, IR) and significant stacking faults (XRD).

■ CONCLUSION

We here reported the synthesis and LT crystal structure of the complete series of layered materials $(C_nH_{2n+1}NH_3)_2MCl_4$ with M = Cu, Mn, Zn and *n* = 6, 7, 12, 13, 16. In their LT form, the main differences between Zn- and Cu-/Mn- materials consist of the nature of the anionic layer (isolated molecular MCl_4 tetrahedra and polymeric 2-D perovskite sheets, respectively) and the relative arrangement of the alkyl ammoniums (interdigitated chains and facing each other, respectively). This translates into a higher temperature of the main phase transition for the Zn-based materials whatever the value of *n*, possibly because of the more rigid surrounding of the alkyl chains. A multitechnique analysis, probing short-, medium-, and long-range orders, showed that in their HT forms, the Zn materials present a high degree of disorder, not only for the alkyl chains as already reported but also for the inorganic layers, again independently of the chain length. For Cu- and Mn-based solids, while the electronic configuration of the metallic cations (d^9 vs d^5) impact the geometry of the MCl_6 octahedra, with Jahn−Teller distortions for M = Cu, this does not significantly affect the thermal properties (temperature and enthalpy of transition), whereas the length of the alkyl chains seem to have a profound impact. For the long-chain materials, phase transitions are associated with slight modifications of the inorganic layer and order−disorder transition of the alkyl chains, especially at the tail, while the organic part is less impacted by the low value of *n*. This dynamic disorder likely favors the appearance of stacking faults that clearly appear for the long-chain materials but are not detected for the short ones. All these differences are of importance for the practical applications of these materials for thermal management. They could for example affect their long-term thermal cycling ability, or translate into different mechanical properties[75] that impact the shaping process, a mandatory step from their integration in practical devices, as currently investigated in our laboratories.[76]

■ ASSOCIATED CONTENT

Supporting Information

The Supporting Information is available free of charge at https://pubs.acs.org/doi/10.1021/acs.chemmater.5c02855.

> Complementary crystallographic information, powder X-ray diffraction, differential scanning calorimetry, X-ray absorption spectroscopy, infrared and Raman spectroscopy, and pair distribution function data for selected compounds (PDF)

Accession Codes

Deposition Numbers 2497694–2497708 contain the supplementary crystallographic data for this paper. These data can be obtained free of charge via the joint Cambridge Crystallographic Data Centre (CCDC) and Fachinformationszentrum Karlsruhe Access Structures service.

■ AUTHOR INFORMATION

Corresponding Authors

Olivier Hernandez – *Nantes Université, CNRS, Institut des Matériaux de Nantes Jean Rouxel, IMN, F-44000 Nantes, France*; Email: olivier.hernandez@cnrs-imn.fr

Grégory Largiller – *Univ. Grenoble Alpes, CEA, LITEN, F-38000 Grenoble, France*; orcid.org/0000-0002-8570-2401; Email: gregory.largiller@cea.fr

Thomas Devic – *Nantes Université, CNRS, Institut des Matériaux de Nantes Jean Rouxel, IMN, F-44000 Nantes, France*; orcid.org/0000-0001-7074-6498; Email: thomas.devic@cnrs-imn.fr

Authors

Côme Archinard – *Univ. Grenoble Alpes, CEA, LITEN, F-38000 Grenoble, France; Nantes Université, CNRS, Institut des Matériaux de Nantes Jean Rouxel, IMN, F-44000 Nantes, France*

Ali Saad – *Univ. Grenoble Alpes, CEA, LITEN, F-38000 Grenoble, France*; orcid.org/0000-0003-0055-2043

Hubert Chevreau – *Synchrotron SOLEIL, Saint-Aubin F-91192 Gif-sur-Yvette, France*

Jean-Yves Mevellec – *Nantes Université, CNRS, Institut des Matériaux de Nantes Jean Rouxel, IMN, F-44000 Nantes, France*

Bernard Humbert – *Nantes Université, CNRS, Institut des Matériaux de Nantes Jean Rouxel, IMN, F-44000 Nantes, France*

Xavier Biquard – *Univ. Grenoble Alpes, CEA, IRIG-MEM, F-38000 Grenoble, France*

Erik Elkaïm – *Synchrotron SOLEIL, Saint-Aubin F-91192 Gif-sur-Yvette, France*

Kenneth Paul Marshall – *Swiss–Norwegian Beamlines at European Synchrotron Radiation Facility, F-38000 Grenoble, France*

Dragos Constantin Stoian – *Swiss–Norwegian Beamlines at European Synchrotron Radiation Facility, F-38000 Grenoble, France*; orcid.org/0000-0002-2436-6483

Wouter Van Beek – *Swiss–Norwegian Beamlines at European Synchrotron Radiation Facility, F-38000 Grenoble, France*

Complete contact information is available at: https://pubs.acs.org/10.1021/acs.chemmater.5c02855

Author Contributions

The manuscript was written through contributions of all authors. All authors have given approval to the final version of the manuscript.

Notes

The authors declare no competing financial interest.

■ ACKNOWLEDGMENTS

The authors acknowledge the synchrotrons Soleil and ESRF for providing access to the CRISTAL and BM31 beamlines, respectively, as well as the French network Reciprocs for the BAG beamtime (Soleil). The BM31 setup was funded by the Swiss National Science Foundation (grant 206021_189629) and the Research Council of Norway (grant 296087). Stéphane Grolleau (IMN), Mathieu Lecointe (IMN), and Nathalie Guillou (ILV) are also thanked for their help in DSC measurements, PXRD data collection, and analysis, respectively.

■ REFERENCES

(1) Mitzi, D. B. Synthesis, Structure, and Properties of Organic-Inorganic Perovskites and Related Materials. In *Progress in Inorganic Chemistry*; Karlin, K. D., Ed.; Wiley, 1999; Vol. *48*, pp 1–121..

(2) Zhang, W.; Zheng, W.; Li, L.; Huang, P.; Xu, J.; Zhang, W.; Shao, Z.; Chen, X. Unlocking the Potential of Organic-Inorganic Hybrid Manganese Halides for Advanced Optoelectronic Applications. *Adv. Mater.* **2024**, *36* (39), 2408777.

(3) Li, X.; Hoffman, J. M.; Kanatzidis, M. G. The 2D Halide Perovskite Rulebook: How the Spacer Influences Everything from the Structure to Optoelectronic Device Efficiency. *Chem. Rev.* **2021**, *121* (4), 2230–2291.

(4) Arend, H.; Hofmann, R.; Waldner, F. New Phase Transition in (CnH2n+1NH3)2MnCl4. *Solid State Commun.* **1973**, *13* (10), 1629–1632.

(5) Landi, E.; Vacatello, M. Metal-Dependent Thermal Behaviour Ln (n-CnH2n+1NH3)2MCl4. *Thermochim. Acta* **1975**, *13* (4), 441–447.

(6) Depmeier, W. The Uniqueness of the Propyl Compound in the Series (CnH2n+1NH3)2MnCl4 with $n = 1{-}10$. *J. Solid State Chem.* **1979**, *29* (1), 15–26.

(7) Busico, V.; Carfagna, C.; Salerno, V.; Vacatello, M.; Fittipaldi, F. The Layer Perovskites as Thermal Energy Storage Systems. *Sol. Energy* **1980**, *24* (6), 575–579.

(8) Busico, V.; Tartaglione, T.; Vacatello, M. Thermal Behaviour of Mixed Long-Chain Alkylammonium Tetrachlorozincates. *Thermochim. Acta* **1983**, *62* (1), 77–86.

(9) He, D.-H.; Di, Y.-Y.; Tan, Z.-C.; Yi, F.-F.; Dan, W.-Y.; Liu, Y.-P. Crystal Structures and Thermochemistry on Phase Change Materials (*n*-CnH2n+1NH3)2CuCl4(s) (n = 14 and 15). *Sol. Energy Mater. Sol. Cells* **2011**, *95* (10), 2897–2906.

(10) Raj, C. R.; Suresh, S.; Bhavsar, R. R.; Singh, V. K.; Reddy, A. S.; Upadhyay, A. Manganese-Based Layered Perovskite Solid–Solid Phase Change Material: Synthesis, Characterization and Thermal Stability Study. *Mech. Mater.* **2019**, *135*, 88–97.

(11) Li, J.; Barrio, M.; Dunstan, D. J.; Dixey, R.; Lou, X.; Tamarit, J.-L.; Phillips, A. E.; Lloveras, P. Colossal Reversible Barocaloric Effects in Layered Hybrid Perovskite (C10H21NH3)2MnCl4 under Low Pressure Near Room Temperature. *Adv. Funct. Mater.* **2021**, *31* (46), 2105154.

(12) Seo, J.; McGillicuddy, R. D.; Slavney, A. H.; Zhang, S.; Ukani, R.; Yakovenko, A. A.; Zheng, S.-L.; Mason, J. A. Colossal Barocaloric Effects with Ultralow Hysteresis in Two-Dimensional Metal–Halide Perovskites. *Nat. Commun.* **2022**, *13* (1), 2536.

(13) Salgado-Pizarro, R.; Svobodova-Sedlackova, A.; Fernández, A. I.; Barreneche, C. Designing Thermal Regulation Materials:

Investigating Alkylamine Length in Polymorphic Layered Hybrid Organic-Inorganic Perovskites. *J. Energy Storage* **2023**, *73*, 109156.

(14) Lopez-Morales, J. L.; Serrano, A.; Centeno-Pedrazo, A.; Perez-Arce, J.; Olmedo-Martinez, J. L.; Casado, N.; Palomo Del Barrio, E.; Garcia-Suarez, E. J. Bis(Dialkylammonium)-Based Hybrid Organic–Inorganic Ionic Materials as Solid–Solid Phase Change Materials. *Chem. Eng. J.* **2024**, *495*, 153501.

(15) Salgado-Pizarro, R.; Navarro-Rivero, M. E.; Ding, Y.; Barreneche, C.; Fernández, A. I. Thermal Evaluation of Polymorphic Transitions in Layered Hybrid Organic-Inorganic Perovskites for Energy Storage Applications. *J. Energy Storage* **2024**, *100*, 113483.

(16) Salgado-Pizarro, R.; Puigjaner, C.; García, J.; Fernández, A. I.; Barreneche, C. Copper- and Manganese-Based Layered Hybrid Organic–Inorganic Compounds with Polymorphic Transitions as Energy Storage Materials. *J. Mater. Chem. A* **2024**, *12* (29), 18544–18553.

(17) Salgado-Pizarro, R.; Mañosa, J.; Barreneche, C.; Fernández, A. I. Synthesis of Bis(Dodecylammonium) Tetrachlorocuprate Using Ball Milling for Thermal Energy Storage. *ACS Sustainable Chem. Eng.* **2025**, *13* (13), 4937–4945.

(18) Matuszek, K.; Kar, M.; Pringle, J. M.; MacFarlane, D. R. Phase Change Materials for Renewable Energy Storage at Intermediate Temperatures. *Chem. Rev.* **2023**, *123* (1), 491–514.

(19) Socías, C.; Arriandiaga, M. A.; Tello, M. J.; Fernández, J.; Gili, P. High-Temperature Phase Transitions in (CnH2n+1NH3)2ZnCl4 Compounds. *Phys. Status Solidi A* **1980**, *57* (1), 405–410.

(20) Kind, R.; Pleko, S.; Arend, H.; Blinc, R.; Seliger, J.; Loar, B.; Slak, J.; Levstik, A.; Filipi, C.; Lahajnar, G.; Milia, F.; Chapuis, G.; Milia, F.; Chapuis, G. Dynamics of the N-decylammonium Chains in the Perovskite-type Layer Structure Compound (C10H21NH3)-2CdCl4. *J. Chem. Phys.* **1979**, *71* (5), 2118–2130.

(21) Zuñiga, F. J.; Chapuis, G. Structural Analysis of the Intermediate Phases of (n-C13H27NH3)2ZnCl4 by Single Crystal Diffraction. *Mol. Cryst. Lid. Cryst.* **1985**, *128* (3–4), 349–366.

(22) Billing, D. G.; Lemmerer, A. Synthesis Characterization and Phase Transitions of the Inorganic–Organic Layered Perovskite-Type Hybrids [(CnH2n+1NH3)2PbI4] (n = 12, 14, 16 and 18). *New J. Chem.* **2008**, *32* (10), 1736–1746.

(23) Lemmerer, A.; Billing, D. G. Synthesis, Characterization and Phase Transitions of the Inorganic–Organic Layered Perovskite-Type Hybrids $[(\mathrm{C}_n\ \mathrm{H}_{2n+1}\ \mathrm{NH}_3)_2\ \mathrm{PbI}_4\ ]$, n = 7, 8, 9 and 10. *Dalton Trans.* **2012**, *41* (4), 1146–1157.

(24) Ferreira, C. F.; Pérez-Cordero, E. E.; Abboud, K. A.; Talham, D. R. Reversible Medium-Dependent Solid–Solid Phase Transformations in Two-Dimensional Hybrid Perovskites. *Chem. Mater.* **2016**, *28* (15), 5522–5529.

(25) Hoshino, N.; Tamura, S.; Akutagawa, T. Negative-to-Positive Thermal Conductivity Temperature Coefficient Transition Induced by Dynamic Fluctuations of the Alkyl Chains in the Layered Complex (C4H9NH3)2CuCl4. *Chem.—Eur. J.* **2020**, *26* (12), 2610–2618.

(26) Lemmerer, A. Thermochromic Phase Transitions of Long Odd-Chained Inorganic–Organic Layered Perovskite-Type Hybrids [(CnH2n+1NH3)2PbI4], n = 11, 13, and 15. *Inorg. Chem.* **2022**, *61* (17), 6353–6366.

(27) Schenk, K. J.; Chapuis, G. Thermotropic Phase Transitions in Bis(n-Tetradecylammonium) Tetrachlorocadmate(II) and Some Homologous Compounds. *J. Phys. Chem.* **1988**, *92* (25), 7141–7147.

(28) Ricard, L.; Rey-Lafon, M.; Biran, C. Vibrational Study of the Dynamics of N-Decylammonium Chains in the Perovskite-Type Layer Compound Decylammonium Tetrachlorocadmate ((C10H21NH3)2CdCl4). *J. Phys. Chem.* **1984**, *88* (23), 5614–5620.

(29) Ricard, L.; Cavagnat, R.; Rey-Lafon, M. Vibrational Study of the Dynamics of N-Alkylammonium Chains in the Perovskite-Type Layer Compounds (CnH2n+1NH3)2CdCl4 (n = 8, 12, 16). *J. Phys. Chem.* **1985**, *89* (22), 4887–4894.

(30) Casal, H. L.; Cameron, D. G.; Mantsch, H. H. A Vibrational Spectroscopic Characterization of the Solid-Phase Behavior of n-Decylammonium Chloride (n-C10H21NH3Cl) and Bis(n-Decylammonium) Tetrachlorocadmate [(n-C10H21NH3)2CdCl4]. *J. Phys. Chem.* **1985**, *89* (25), 5557–5565.

(31) Ba Chanh, N.; Hauw, C.; Meresse, A.; Rey-Lafon, M.; Ricard, L. X-Ray Diffraction, Differential Scanning Calorimetric and Spectroscopic Studies of Phase Transitions in the Bidimensional Compound (C12H25NH3)2CdCl4. *J. Phys. Chem. Solids* **1985**, *46* (12), 1413–1420.

(32) Almirante, C.; Minoni, G.; Zerbi, G. Mechanism of Solid to Liquidlike Phase Transition of Alkyl Chains in Bilayer Systems. An Infrared Spectroscopic Study of Tetradecylammonium Tetrachloromanganate ([CH3(CH2)13NH3]2MnCl4) and Tetradecylammonium Tetrachlorozincate [CH3(CH2)13NH3]2ZnCl4. *J. Phys. Chem.* **1986**, *90* (5), 852–859.

(33) Kang, J.-K.; Choy, J.-H.; Rey-Lafon, M. Phase Transition Behavior in the Perovskite-Type Layer Compound (n-C12H25NH3)-2CuCl4. *J. Phys. Chem. Solids* **1993**, *54* (11), 1567–1577.

(34) Rey-lafon, M.; Lartigue-bourdeau, C.; Maris, Th.; Khechoubi, M.; Chanh, N. B. Spectroscopic and Crystallographic Study of Phase Transitions in Zn Bidimensional Complexes. *Mol. Cryst. Lid. Cryst.* **1995**, *269* (1), 55–73.

(35) Kammoun, S.; Kamoun, M.; Daoud, A.; Romain, F. Differential Scanning Calorimetric, x-Ray Diffraction, and Spectroscopic Studies of Phase Transitions in the Two-Dimensional Compound (C6H13NH3)2PbCl4. *Phys. Status Solidi A* **1996**, *156* (2), 317–329.

(36) Ning, G. Characterization of the Solid-Phase Behavior of *n*-Nonylammonium Tetrachlorocuprate by Fourier Transform Infrared Spectroscopy. *J. Solid State Chem.* **1995**, *117* (1), 97–102.

(37) Blinc, R.; Burgar, M. I.; Rutar, V.; Žekš, B.; Kind, R.; Arend, H.; Chapuis, G. Phase Transitions in a Lipid Bilayer Embedded in a Crystalline Matrix. *Phys. Rev. Lett.* **1979**, *43* (22), 1679–1682.

(38) Lim, A. R. Thermal Property, Structural Characterization, and Physical Property of Cation and Anion in Organic–Inorganic Perovskite [(CH2)3(NH3)2]CdCl4 Crystal. *J. Solid State Chem.* **2021**, *295*, 121909.

(39) Kim, A. Y.; Na, C.; Lim, A. R. Crystal Structures, Phase Transitions, Thermodynamics, and Molecular Dynamics of Organic–Inorganic Hybrid Crystal [NH(CH3)3]2ZnCl4. *Sci. Rep.* **2024**, *14* (1), 3441.

(40) Lim, A. R. Refined Analysis of the Crystal Structure, Thermodynamic Property, and Structural Geometry of Perovskite (CH3NH3)2ZnBr4. *ACS Omega* **2024**, *9* (43), 43908–43913.

(41) Guillaume, F.; Coddens, G.; Dianoux, A. J.; Petry, W.; Rey-Lafon, M.; Sourisseau, C. Molecular Motions of Decylammonium Chains in the Perovskite Type Layered Compound (C10H21NH3)-2MnCl4: An Incoherent Neutron Scattering Study. *Mol. Phys.* **1989**, *67* (3), 665–679.

(42) Avitabile, G.; Ciajolo, M. R.; Napolitano, R.; Tuzi, A. Comparative Studies of Layer Structures: The Crystal Structures of Bis(Mono-n-Dodecylammonium) Tetrabromozincate and Bis(Mono-n-Tridecylammonium) Tetrabromozincate. *Gazz. Chim. Ital.* **1983**, *113*, 475–479.

(43) Liu, Y.; Di, Y.; He, D.; Zhou, Q.; Dou, J. Crystal Structures, Lattice Potential Energies, and Thermochemical Properties of Crystalline Compounds (1-CnH2n+1NH3)2ZnCl4(s) (n = 8, 10, 12, and 13). *Inorg. Chem.* **2011**, *50* (21), 10755–10764.

(44) Sheldrick, G. M. Crystal Structure Refinement with SHELXL. *Acta Cryst. C* **2015**, *71* (1), 3–8.

(45) Dolomanov, O. V.; Bourhis, L. J.; Gildea, R. J.; Howard, J. A. K.; Puschmann, H. OLEX2: A Complete Structure Solution, Refinement and Analysis Program. *J. Appl. Crystallogr.* **2009**, *42* (2), 339–341.

(46) Petříček, V.; Palatinus, L.; Plášil, J.; Dušek, M. Jana2020 – a New Version of the Crystallographic Computing System Jana. *Z. Kristallo. Cryst. Mater.* **2023**, *238* (7–8), 271–282.

(47) Boultif, A.; Louër, D. Powder Pattern Indexing with the Dichotomy Method. *J. Appl. Crystallogr.* **2004**, *37* (5), 724–731.

(48) Rodriguez-Carvajal, J. Fullprof Suite. *Phy. B* **1993**, *192*, 55.

(49) *Topas V5: General Profile and Structure Analysis Software for Powder Diffraction Data*, 2014.

(50) Favre-Nicolin, V.; Černý, R. F. O. X. ‘free Objects for Crystallography’: A Modular Approach to Ab Initio Structure Determination from Powder Diffraction. *J. Appl. Crystallogr.* **2002**, *35* (6), 734−743.

(51) Dyadkin, V.; Pattison, P.; Dmitriev, V.; Chernyshov, D. A New Multipurpose Diffractometer PILATUS@SNBL. *J. Synchrotron Rad.* **2016**, *23* (3), 825−829.

(52) Ravel, B.; Newville, M. ATHENA, ARTEMIS, HEPHAESTUS Data Analysis for X-Ray Absorption Spectroscopy Using IFEFFIT. *J. Synchrotron Rad.* **2005**, *12* (4), 537−541.

(53) Rehr, J. J.; Kas, J. J.; Vila, F. D.; Prange, M. P.; Jorissen, K. Parameter-Free Calculations of X-Ray Spectra with FEFF9. *Phys. Chem. Chem. Phys.* **2010**, *12* (21), 5503−5513.

(54) Kas, J. J.; Vila, F. D.; Pemmaraju, C. D.; Tan, T. S.; Rehr, J. J. Advanced Calculations of X-Ray Spectroscopies with FEFF10 and Corvus. *J. Synchrotron Rad.* **2021**, *28* (6), 1801−1810.

(55) Alonso, J. A.; Martínez-Lope, M. J.; Casais, M. T.; Fernández-Díaz, M. T. Evolution of the Jahn−Teller Distortion of MnO6 Octahedra in RMnO3 Perovskites (R = Pr, Nd, Dy, Tb, Ho, Er, Y): A Neutron Diffraction Study. *Inorg. Chem.* **2000**, *39* (5), 917−923.

(56) McNulty, J. A.; Lightfoot, P. Structural Chemistry of Layered Lead Halide Perovskites Containing Single Octahedral Layers. *IUCrJ* **2021**, *8* (4), 485−513.

(57) Liu, T.; Holzapfel, N. P.; Woodward, P. M. Understanding Structural Distortions in Hybrid Layered Perovskites with the n = 1 Ruddlesden−Popper Structure. *IUCrJ* **2023**, *10* (4), 385−396.

(58) Choy, J.-H.; Kang, J.-K.; Park, J.-C.; Chanh, N.-B.; Rey-Lafon, M. Thermotropic Phase Transitions in the Bidimensional Compound $(C_{10}\ H_{21}\ NH_3)_2$ Cucl$_4$. *J. Chim. Phys.* **1993**, *90*, 1829−1854.

(59) Socias, C.; Arriandiaga, M. A.; Tello, M. J.; Fernandez, J.; Gili, P. High-Temperature Phase Transitions in (CnH2n+1NH3)2ZnCl4 Compounds. *Phys. Status Solidi* **1980**, *57*, 405−410.

(60) Coelho, A. A.; Evans, J. S. O.; Lewis, J. W. Averaging the Intensity of Many-Layered Structures for Accurate Stacking-Fault Analysis Using Rietveld Refinement. *J. Appl. Crystallogr.* **2016**, *49*, 1740−1749.

(61) Fedoruk, K.; Drozdowski, D.; Maczka, M.; Zareba, J. K.; Stefańska, D.; Gagor, A.; Sieradzki, A. [Methylhydrazinium]2PbCl4, a Two-Dimensional Perovskite with Polar and Modulated Phases. *Inorg. Chem.* **2022**, *61* (39), 15520−15531.

(62) Ferrandon, M.; Daggupati, V.; Wang, Z.; Naterer, G.; Trevani, L. Using XANES to Obtain Mechanistic Information for the Hydrolysis of CuCl2 and the Decomposition of Cu2OCl2 in the Thermochemical Cu−Cl Cycle for H2 Production. *J. Therm. Anal. Calorim.* **2015**, *119* (2), 975−982.

(63) Lysenko, V. Yu.; Kremennaya, M. A.; Yalovega, G. E. Local Atomic Environment of Zn2+ Ions in a Low-Concentration ZnCl2 Aqueous Solution: XANES Study. *Crystallogr. Rep.* **2023**, *68* (2), 242−246.

(64) Ye, C.; McHugh, L. N.; Florian, P.; Yu, R.; Castillo-Blas, C.; Chen, C.; Lang, A.; Dai, Y.; Hou, J.; Keen, D. A.; Dutton, S. E.; Bennett, T. D. Structural Dynamics of Melting and Glass Formation in a Two-Dimensional Hybrid Perovskite. *Nat. Commun.* **2025**, *16* (1), 7696.

(65) Zhong, W.-W.; Di, Y.-Y.; Kong, Y.-X.; Lu, D.-F.; Dou, J.-M. Lattice Potential Energies and Thermochemical Properties of Phase Change Materials (1-C*n*H2*n*+1NH3)2MnCl4(s) (*n* = 10 and 11). *J. Chem. Thermodyn.* **2014**, *72*, 100−107.

(66) Maroncelli, M.; Qi, S. P.; Strauss, H. L.; Snyder, R. G. Nonplanar Conformers and the Phase Behavior of Solid N-Alkanes. *J. Am. Chem. Soc.* **1982**, *104* (23), 6237−6247.

(67) Beattie, I. R.; Gilson, T. R.; Ozin, G. A. Single-Crystal Raman Spectroscopy of ‘Square-Planar’ and ‘Tetrahedral’ CuCl42− Ions, of the ZnCl42− Ion, and of CuCl2,2H2O. *J. Chem. Soc. A* **1969**, *0* (0), 534−541.

(68) Iqbal, Z.; Arend, H.; Wachter, P. Raman Scattering from Layer-Type Magnets: $(CH_2)_n$ $(NH_3)_2$ $CuCl_4$, N = 2, 3 and 5. *J. Phys. C: Solid State Phys.* **1980**, *13* (25), 4757−4767.

(69) Pabst, I.; Karolyi, J.; Fuess, H.; Couzi, M. Phase Sequence of [CH3NH3]2CuCl4 Studied by X-Ray Diffraction and Low-Frequency Raman Scattering. *Phys. Status Solidi A* **1996**, *155* (2), 341−352.

(70) Zulfa, K.; Zahara, B.; Akmal Afkauni, A.; Yuniar Diah Maulida, P.; Hartati, S.; Mulyani, I.; Yudhowijoyo, A.; Jaya Diguna, L.; Haris Mahyuddin, M.; Onggo, D.; Danang Birowosuto, M. Arramel. Elucidating the Vibration Modes of Two-Dimensional Hybrid Copper Halide Perovskite Crystals by FTIR and Raman Spectroscopy. *Mater. Today: Proc.* **2024**, In press .

(71) Wong, P. T. T. Raman Spectra of Single- and Polycrystalline Cs2[ZnCl4] Complex. *J. Chem. Phys.* **1976**, *64* (5), 2186−2191.

(72) Zhu, H.; Huang, Y.; Ren, J.; Zhang, B.; Ke, Y.; Jen, A. K.-Y.; Zhang, Q.; Wang, X.-L.; Liu, Q. Bridging Structural Inhomogeneity to Functionality: Pair Distribution Function Methods for Functional Materials Development. *Adv. Sci.* **2021**, *8* (6), 2003534.

(73) Terban, M. W.; Billinge, S. J. L. Structural Analysis of Molecular Materials Using the Pair Distribution Function. *Chem. Rev.* **2022**, *122* (1), 1208−1272.

(74) Famprikis, T.; Bouyanfif, H.; Canepa, P.; Zbiri, M.; Dawson, J. A.; Suard, E.; Fauth, F.; Playford, H. Y.; Dambournet, D.; Borkiewicz, O. J.; Courty, M.; Clemens, O.; Chotard, J.-N.; Islam, M. S.; Masquelier, C. Insights into the Rich Polymorphism of the Na+ Ion Conductor Na3PS4 from the Perspective of Variable-Temperature Diffraction and Spectroscopy. *Chem. Mater.* **2021**, *33* (14), 5652−5667.

(75) Houghton, O. S.; Ye, C.; Twitchett-Harrison, A. C.; Dutton, S. E.; Bennett, T. D.; Greer, A. L. Glass Transition, Liquid Dynamics, and Thermal Degradation in 2D Hybrid Halide Perovskites. *Small* **2025**, *21* (19), 2500311.

(76) Saad, A.; Archinard, C.; Weick, C.; Pietri, T.; Hernandez, O.; Devic, T.; Largiller, G. From scalable synthesis to thermal integration: a comprehensive assessment of a hybrid solid−solid PCM for Li-ion battery applications. in revision.